ISSN online 2545-2819
ISSN print 0800-6377

DOI: 10.2478/ncr-2018-0012

Received: March 28, 2018
Revision received: Nov. 20, 2018
Accepted: Nov. 28, 2018

Meso Mechanical Study of Cracking Process in Concrete Subjected to Tensile Loading

Mathias Flansbjer
M.Sc., Ph.D., Adj. Prof., Researcher
RISE Research Institutes of Sweden, Mechanics Research
Box 857 SE-501 15 Borås, Sweden
E-mail: mathias.flansbjer@ri.se

Jan Erik Lindqvist
Ph.D., Senior researcher
RISE Research Institutes of Sweden, CBI
Ideon, SE-223 70 Lund, Sweden
E-mail: janerik.lindqvist@ri.se

ABSTRACT
This project focused on how the cracking process in concrete is influenced by both the micro and meso structures of concrete. The aim was to increase knowledge pertaining to the effect of critical parameters on the cracking process and how this is related to the material's macroscopic properties. A methodology based on the combination of different experimental methods and measuring techniques at different scales was developed. Crack propagation during tensile loading of small-scale specimens in a tensile stage was monitored by means of Digital Image Correlation (DIC) and Acoustic Emission (AE). After testing, crack patterns were studied using fluorescence microscopy.

Key words: Concrete, Cracking, Testing, Digital Image Correlation, Acoustic Emission, Microscopic Analysis

1. INTRODUCTION

Many of the characteristics of concrete mechanical behaviour observed at the macro scale can be explained by the heterogeneous structure of concrete at the micro and meso scales. Conventional strength tests on the macroscopic scale are essentially intended to characterize and compare different qualities of concrete in a standardized way but give limited information at the micro and meso scales since they do not reflect the heterogeneous nature of the materials in a relevant way. Therefore, the combination of different experimental methods and measuring techniques at different scales is essential to enable deep investigation and understanding of the cracking process from micro to macro scale. Within this project, we focus on how the fracture process in concrete is influenced by the aggregate shape. The project includes the development of a methodology that enables detailed analysis at the micro and meso scales. The methodology is based on the combination of different experimental methods and measuring techniques on different scales, see Figure 1.

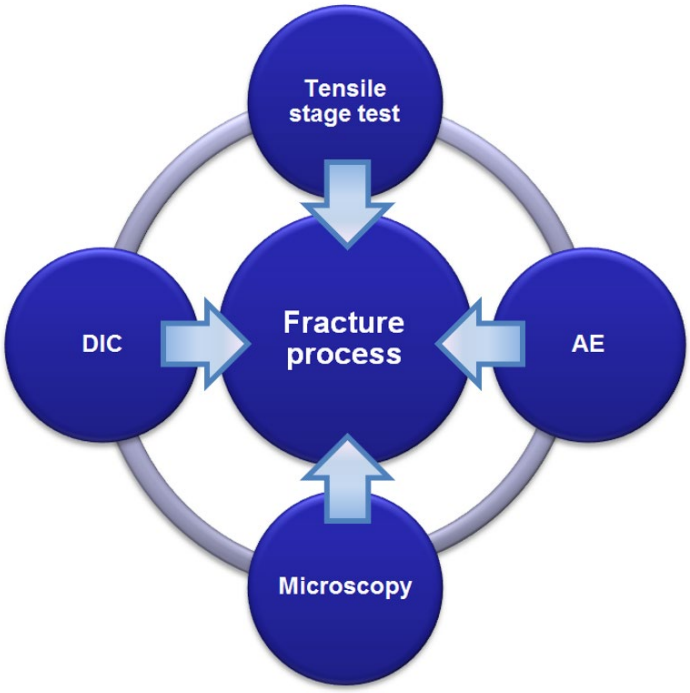

Figure 1 – Experimental methodology.

In the small-scale tests, concrete specimens were subjected to a direct tensile force in a tensile stage, while the fracture process was registered by Digital Image Correlation (DIC) and Acoustic Emission (AE). Both techniques have been used comprehensively to study the cracking process in concrete, but only a few papers have highlighted the potential to use them in combination, e.g. [1-3]. By using DIC it is possible to follow crack propagation in relation to the material structure on the surface of the specimen in a detailed way, whereas AE offers real-time measurement of the crack activity within the specimen. By combining these techniques, it is possible to relate the AE signal characteristics to different phases of the cracking process, such

as crack initiation, propagation and bridging of microcracks into macrocracks, as well as the creation and localization of the final fracture. The specimens were impregnated with epoxy containing fluorescent dye in their final state after testing. The cracks and final fractures were then microscopically examined, which allowed to link the cracking and fracturing processes to the textures and microstructures of the concrete. A similar methodology was presented in [4], based on the combination of DIC and examination of epoxy impregnated specimens in the study of fracture process of concrete in compression.

2. METHODS FOR FRACTURE CHARACTERIZATION

2.1 Digital Image Correlation

In recent years, there has been a substantial development of optical full-field deformation measurement systems based on Digital Image Correlation (DIC). Originally developed in the 1980s, this technique has been successfully applied to various mechanical and civil engineering structural problems [5]. This measurement technique is typically used to measure displacement fields and surface strain fields both in 2D and 3D. The basic idea behind DIC is to measure the displacement of the given specimen during testing by tracking the deformation of a naturally occurring or applied surface speckle pattern in a series of digital images acquired during loading. The analysis of the displacement of discrete pixel subsets of the speckle pattern within the images enables the acquisition of these data. As cracks are characterized by discontinuities in the displacement field, DIC measurements have proved suitable for the monitoring of crack formations in concrete at different scales, as previously shown by e.g. [4, 6-14]. It is possible to follow the propagation of all individual cracks at the surface long before they are visible to the naked eye, and subsequently quantify the crack width development locally for each crack with high accuracy until failure. By using the natural pattern of sawn specimen surfaces, cracking and crack growth can be monitored in detail in relation to the micro- and meso structures of the concrete.

In this study, the crack propagation was registered in a detailed way at different scales by 2D measurements at the surface of the specimens during testing by using the optical full-field deformation measurement system ARAMIS^{TM} 4M by GOM.

2.2 Acoustic Emission

Acoustic Emission (AE) monitoring is a pertinent technique for monitoring fracture processes in concrete, both on material and structural levels, e.g. [3, 15-21]. The method is based on the small elastic stress waves produced by sudden movements in stressed materials caused by crack initiation and growth. A sudden movement at the source triggers the release of energy, in the form of stress waves, which radiate out into the structure and are recorded by sensors at the surface. The AE measurement system simply listens for the energy released by the object. This type of AE often has very small amplitudes and is in principle always of high frequency. Typical frequencies that are optimal for AE measurements can be within the range of 60–300 kHz. AE is therefore measured with highly sensitive piezoelectric resonant sensors in the ultrasonic range. The key element in an AE resonant sensor is the piezoelectric crystal that converts the movements into electrical voltage signals that are sent to a measuring computer for further signal processing. Various parameters are used to identify the nature of the AE source, including hits, events, counts, duration, amplitude, rise-time, energy and frequency.

AE monitoring offers real-time measurement of crack formation and is not limited to a single measuring point, as it is volumetric. AE monitoring can detect crack initiation and crack growth and provide information on when damage is accelerating. Furthermore, if an AE signal reaches several sensors and the speed of sound is known, the approximate location of the event can be determined.

In this study, a six-channel Micro-II Digital AE system by Physical Acoustics Corporation was used for measuring and analysing AE. The system basically consists of AE sensors, pre-amplifiers and a PC for data acquisition, signal processing and analysis.

2.3 Micro and meso scale analysis

The analyses of the tested samples were performed using fluorescence microscopy on thin sections impregnated with epoxy containing fluorescent dye. The analysed thin sections were cut parallel to the surface analysed using DIC. The size of the thin sections was approximately 70×50 mm^2 with their length axis oriented parallel to the main cracks. The measurements were performed using the KS400 image analysis program on images covering an area of 5.5×4.2 mm^2. Six to nine images were taken covering 33 to 50 mm of the length of the fracture zone. The fracture surfaces were classified as fractures in aggregate, paste and intertransitional zone (ITZ) adjacent to the aggregate. The classification was done manually while the quantitative measurements were made using image analysis. Each side of the fractures were analyzed separately.

The parameter used to describe aggregate particle shape was the minimum length divided by the maximum length (F_{min}/F_{max}) To reduce stereological artefacts, half of the objects with the lowest F_{max} was excluded from the measurement. This rule was used in order to be scale independent. Generally, these were objects with an F_{max} smaller than about 100 microns. Eighty percent of the remaining measured particles were in the size range 0.25 to 2 mm assessed according to [22]. In this measurement, objects with F_{min}/F_{max} larger than 0.6 as well as edge-objects were excluded. For further information the reader is referred to [23].

3. MATERIAL DESCRIPTION

The test series presented in this work included two different concrete recipes, referred to as N038 and C038. The concretes had a w/c of about 0.38 and the coarse aggregate (8-16 mm) consisted of felsic rock material. The main difference between the mixes was related to the fine aggregate (< 8 mm), which were of Natural (N038) or Crushed (C038) felsic rock material. The compressive cube strengths at 28 days were determined to be 91.5 MPa and 80.9 MPa for N038 and C038, respectively. Furthermore, the tensile strength and fracture energy were determined by direct tensile tests on notched cube specimens according to recommendations given by RILEM [24] and [25]. A summary of the material properties is given in Table 1. The same materials, cast at the same time, were used in an earlier project concerning factors affecting the shear strength capacity based on an understanding of micro and meso scale material properties [10].

Table 1 – Material description.

Parameter	C038	N038
w/c	0.38	0.38
Fine aggregate 0-8 mm [kg/m^3]	1060	900
Coarse aggregate 8-16 mm [kg/m^3]	708	900
Water [kg/m^3]	164	162
Cement [kg/m^3]	429	426
Water reducer [kg/m^3]	1.1	0.7
Compressive cube strength [MPa]	80.9	91.5
Tensile strength [MPa]	5.0	5.2
Fracture energy [N/m]	209	176

The frequency distribution of the aggregate shapes for crushed and natural aggregate is shown in Figure 2. It can be observed from this figure that the crushed aggregate in the 0.25 to 4 mm fraction contains a significantly higher amount of elongated and flaky particles, i.e. low F_{min}/F_{max}, compared to the rounded natural aggregate particles. Quantitative microscopic analysis of the fine aggregate particles indicated a significant orientation in most of the analysed micro images. The orientation of the aggregate differs however between different micro images (2.8×2.1 mm^2) and there is no orientation that is consistent within the area of a thin section (70×50 mm^2). This pattern with orientation in the microscale but not in the mesoscale occurs in samples with both natural and crushed aggregate.

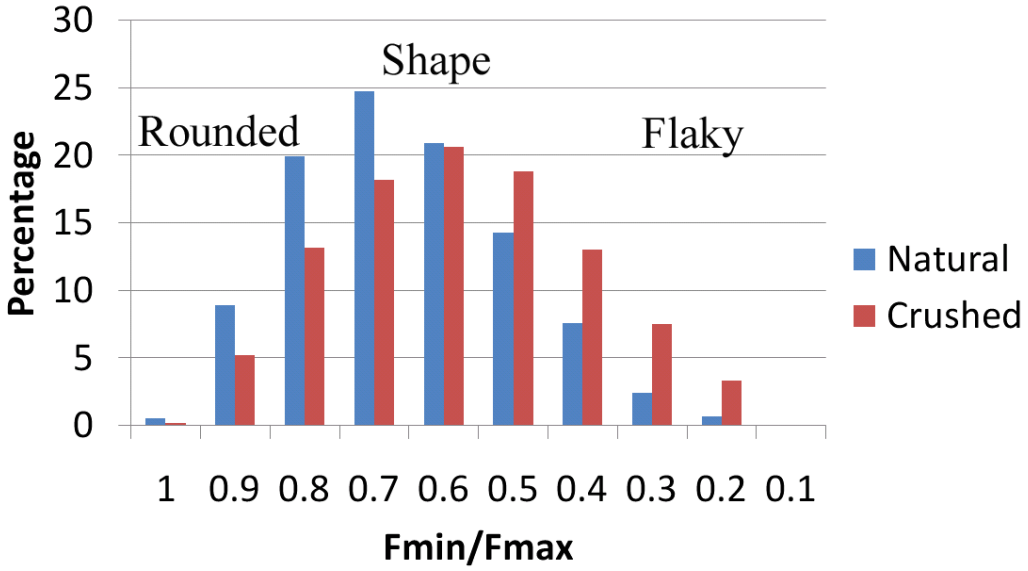

Figure 2 – Shape factor distribution for the natural and crushed fine aggregate used.

4. DIRECT TENSILE TESTS

4.1 Specimen preparation

Rectangular prisms with section dimensions of 60 × 60 mm^2 were cut from cast concrete blocks according to the illustration in Figure 3 (left). The top and bottom edges were face-ground to the

final length to achieve plane parallel surfaces. Along the two sides, a 10 mm deep and 5 mm wide notch was cut with a stationary diamond cutting blade. Finally, the prisms were cut into the test specimens with geometry as shown in Figure 3 (right). Specimens with two different thicknesses *t* were manufactured, i.e. 10 and 20 mm. The specimens with Natural and Crushed fine aggregates are referred to as N038-# and C038-#, respectively.

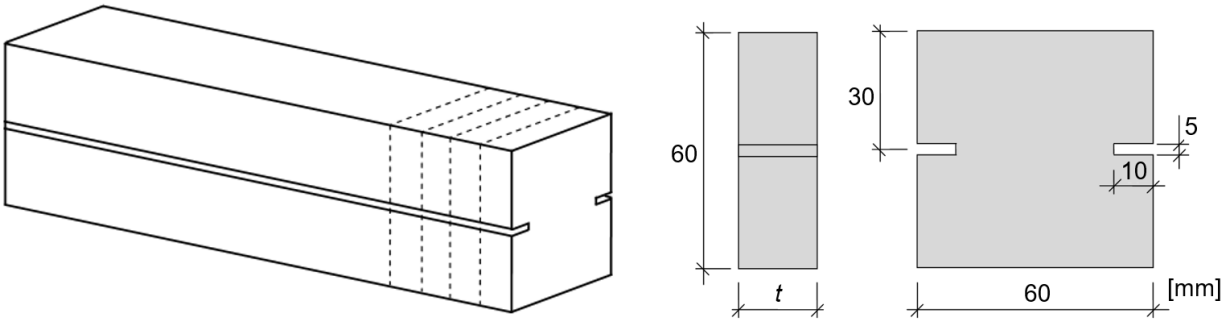

Figure 3 – Specimen preparation and geometry.

To make the meso structure of the concrete more prominent in the DIC images, the surface of the specimens was polished in several steps (Table 2) in a grinding machine before testing.

Table 2 – Surface preparation in Abramin grinding machine from Struers.

Step	SiC Paper	Lubricant	Force [N]	Speed [rpm]	Time [min]
1	220	water	200	300	3-5
2	500	water	200	300	3
3	1000	water	200	300	3
4 [1)]	4000	water	200	300	5

1) This step was only performed when microscope objective was used during testing.

The specimen was glued to the two loading platens of the machine, see Figure 4. Thereby, any small deviations from parallelism between the specimen end surfaces and the loading platens were accommodated by the adhesive layer yielding a perfect fit between the specimen and the loading platens. The specimen was glued to the upper loading platen using a fixture to ensure that the centre lines of the platen and the specimen coincided and to ensure that the face of the loading platen and the centre axis of the specimen were positioned perpendicularly. The upper loading platen, together with the glued-on specimen, was then bolted to the machine. Finally, the lower loading plate, which was already attached to the machine, was glued to the bottom of the specimen. The maximum difference in adhesive thickness over the area was approximately 0.1 mm. The adhesive used was X60 by HBM. Before gluing, the contact surfaces of the specimen and loading platens were cleaned with abrasive paper and acetone to ensure good adhesion. The adhesive could set for at least 30 minutes before testing.

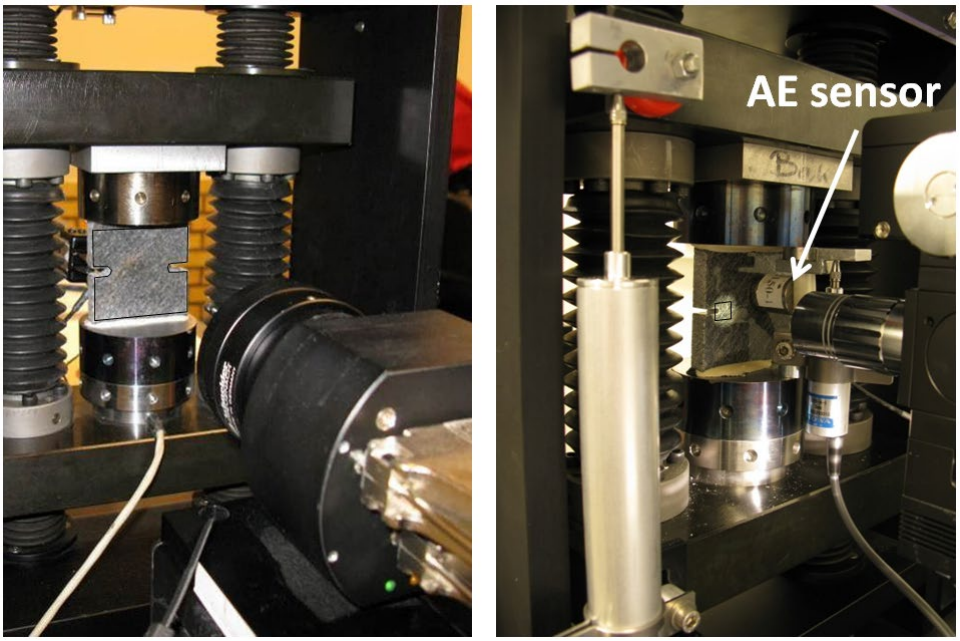

Figure 4 – Photo of tensile stage test setup with camera configuration at meso scale (left) and at micro scale (right).

4.2 Test setup and performance

The direct tensile test setup consisted of different subsystems as illustrated in Figure 5; the tensile stage with control system, data acquisition system, AE system and DIC system.

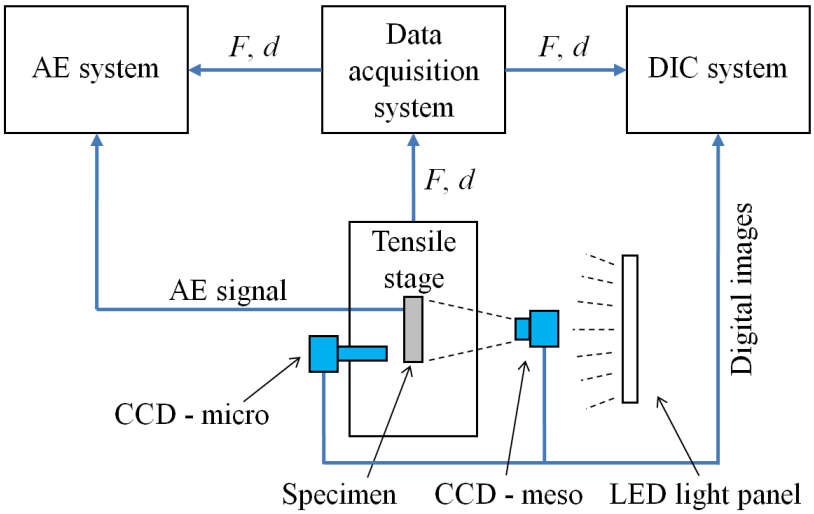

Figure 5 – Illustration of the tensile stage test system.

The tensile stage can be considered as a small mechanical testing machine. Two cross beams are connected to each other by two high-precision right- and left-handed roller screws. When the screws rotate, the two cross beams move away from/toward each other symmetrically relative to the centre line. As such, the centre of the specimen remains in the centre of the digital image during the entire test. The screws are rotated by an ABB brushless servomotor. The force F was recorded by a load cell with a maximum capacity of 10 kN and the relative displacement d between the two cross beams was measured with a LVDT with a measuring range of ±5.0 mm.

Furthermore, the displacement was measured locally over the two notches by Crack Opening Displacement (COD) transducers, COD_1 and COD_2, with a gauge point distance of approximately 5 mm. The steel brackets used to hold the two COD transducers in position were mounted on each side of the notches with a fast-curing adhesive. The COD transducers had a measuring range of 4.0 mm and a relative error of less than 1 %. In these tests, the loading was controlled at a displacement rate of 0.06 mm/min. Photos of the test set-up are shown in Figure 4.

The setup enables 2D DIC measurements on two different scales: one meso scale covering the entire specimen surface (65 × 65 mm^2) and one micro scale focusing on one of the notches covering an area of 8 × 8 mm^2, see Figure 6. At the meso scale, the sub-set size was 20 × 20 pixels and the overlap was three pixels, and at the micro scale, the sub-set size was 50 × 50 pixels and the overlap was 20 pixels. The system setup employed resulted in a spatial resolution of approximately 0.63 × 0.63 mm and 0.19 × 0.19 mm, and a coordinate measurement accuracy of approximately 1.3 µm and 0.16 µm, for the meso and the micro scales, respectively. To obtain high contrast levels, the specimen was illuminated by a white LED light panel at the meso scale. The images were captured with a frequency of 5 Hz. The AE activity was recorded by one AE sensor with a resonance frequency of 150 kHz, see Figure 5 (right). A pre-amplification of 40 dB and a threshold level of 40 dB were used. The hit detection parameters were set to: PDT = 100 µs, HDT = 200 µs and HLT = 200 µs. The force and the displacement were also recorded in the DIC and the AE systems.

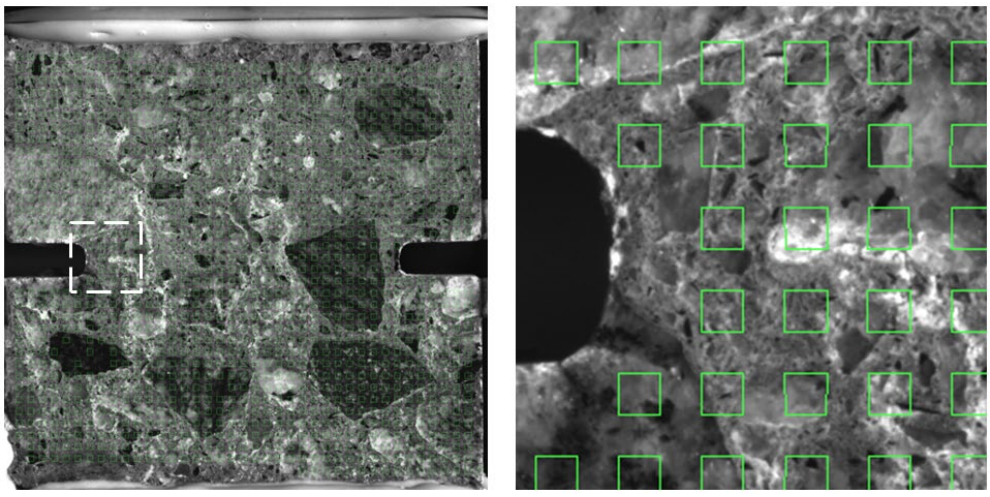

Figure 6 – DIC image with sub-sets at meso scale (left) and at micro scale (right). The image size is 65×65 mm^2 and 8×8 mm^2, respectively.

5. EXPERIMENTAL RESULTS

The tensile behaviour of the concrete was evaluated from small-scale direct tensile tests, as described in Section 4.1. For each material three specimens had a thickness of approximately 20 mm and six specimens had a thickness of approximately 10 mm. The performed tests are summarized in Table 3 and the tensile stress-displacement relationships are shown in Figure 7. The displacement is represented as the mean value of the two COD transducers. The ligament area is the measured section of the location of the notch. The maximum tensile stress along with the corresponding crack opening displacement are summarized in Table 3.

Table 3 – Summary of the small-scale direct tensile tests.

Specimen	Thickness [mm]	Ligament area [mm^2]	DIC scale	Max. tensile stress [MPa]	COD at max tensile stress [μm]
N038-1	20.2	8.2	Meso	4.5	13
N038-2	20.5	7.9	Meso	4.5	11
N038-3	19.7	7.9	Meso	5.2	11
N038-4	10.2	4.3	Meso	4.8	9
N038-5	10.2	4.3	Meso	4.2	13
N038-6	9.9	4.2	Meso	5.7	11
N038-7	9.9	4.2	Micro	5.1	14
N038-8	9.9	4.1	Micro	6.3	13
N038-9	10.1	4.2	Micro	6.1	9
C038-1	20.7	8.5	Meso	5.7	-
C038-2	20.5	8.4	Meso	4.6	11
C038-3	20.6	8.5	Meso	4.9	12
C038-4	10.1	4.1	Meso	4.7	12
C038-5	10.0	4.0	Meso	4.7	11
C038-6	10.1	4.0	Meso	5.2	11
C038-7	10.1	4.0	Micro	5.3	5
C038-8	10.0	4.0	Micro	4.2	8
C038-9	10.2	4.1	Micro	5.6	10

In general, no major differences were found in stress-displacement relationships or crack formation during testing between the specimens with a thickness of 20 mm and those with a thickness of 10 mm. The more detailed analyses by DIC, AE and microscopy were therefore limited to the thinner specimens, N038-4 to N038-9 and C038-4 to C038-9.

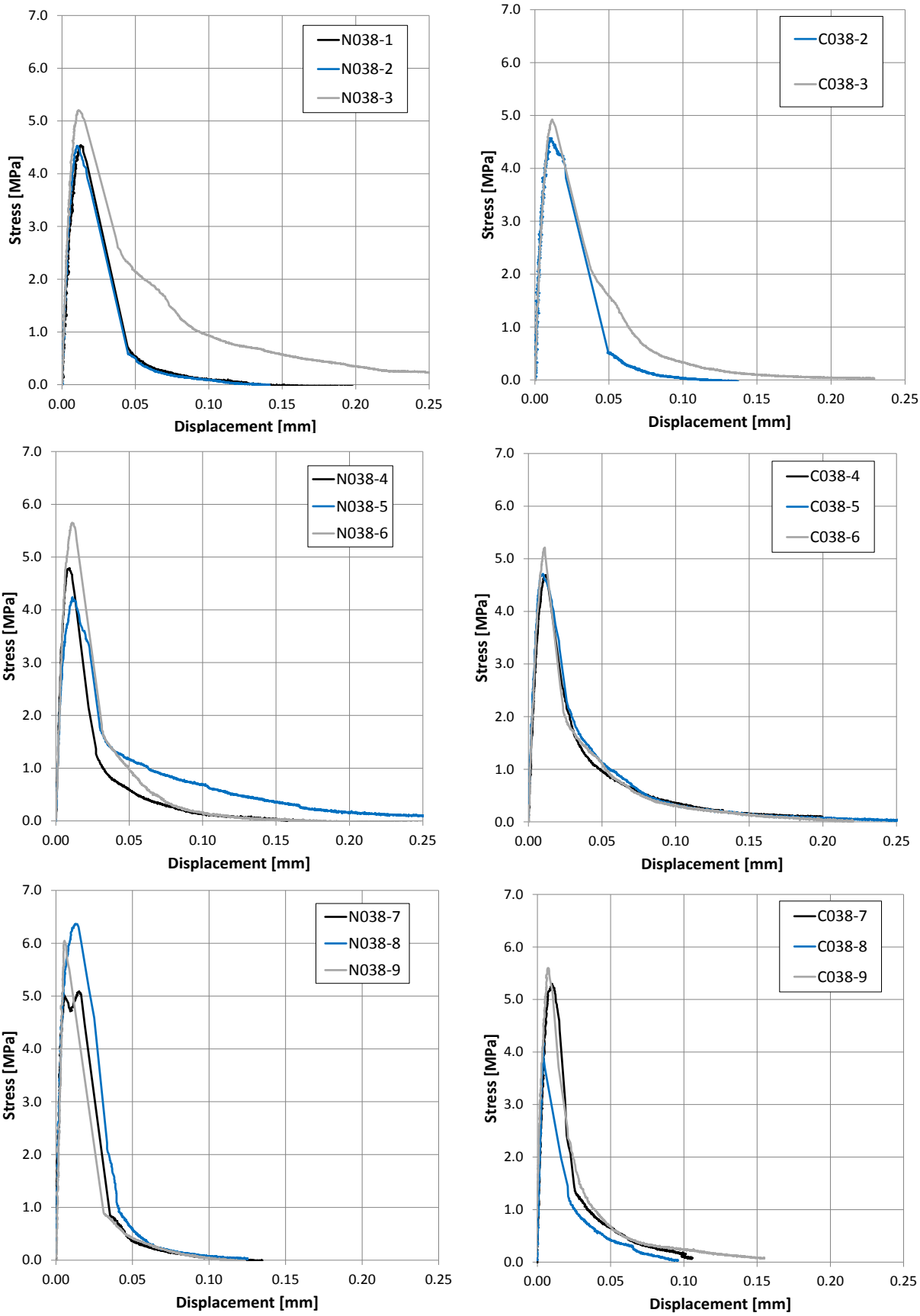

Figure 7 – Tensile stress vs. displacement from direct tensile tests on notched small-scale concrete specimens.

Instead of using the COD transducers to measure the deformation over the notched area, it is also possible to use "virtual" extensometers in the DIC measurements. For C038-5 a comparison between the results obtained by the transducers and the "virtual" extensometers (C038-5 DIC) is shown in Figure 8. The displacement determined by DIC was calculated as the mean value of two virtual extensometers (COD1 and COD2), see Figure 9. Initially, the correspondence between the displacements evaluated from the COD transducers and from DIC measurements is reasonable. Results start to differ close to peak stress and during the descending branch; displacements evaluated from the DIC give smaller values compared to the COD transducers. This applies to all compared specimens and is related to the fact that the displacement is measured closer to the bottom of the notch by DIC. Hence, the deformation over the notched area can be evaluated from the DIC measurements, which would considerably simplify the test method as the COD transducers can be excluded.

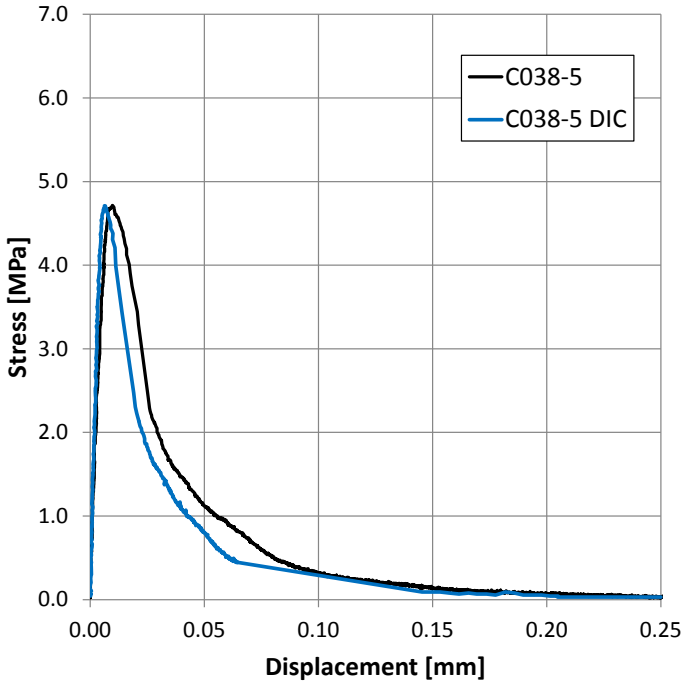

Figure 8 – Comparison of tensile stress vs. displacement measured by COD transducers and by virtual extensometers in DIC.

The methodology allows the cracking process to be monitored by DIC in relation to the texture of the concrete, both on the meso and micro scales. The small discontinuities related to crack formations can be clearly visualized by overlaying major strain fields at the surface of the specimen. Figure 9 (right) presents the crack formation obtained by DIC at different phases of the loading for specimen C038-5. In general, the quality of DIC measurements is strongly influenced by the speckle pattern used; hence, the use of natural speckle pattern may cause some limitations. The texture of the polished concrete in this study was relatively suitable but included some larger areas with minor differences in greyscale; thus, leading to deteriorated results in these areas. To some extent this could be amended by using larger subsets, although it would also reduce the spatial resolution. Hence, the size and step size of the subsets were chosen based on the material texture used as pattern and the desired resolution and accuracy.

In this study, the analysis of the AE signals was limited to hits, which gives an indication of crack initiation and crack intensity. In the hits-displacement relationship presented for specimen

C038-5 in Figure 9 (left) one can see that the AE activity, represented as cumulative number of hits, was relatively small during the pre-peak part compared to during the post-peak part. Also, the amplitude of the hits differs between the two parts, with an average value of approximately 45 dB in the pre-peak part and approximately 50 dB in the post-peak part. These observations were general for all specimens. It should be kept in mind that the obtained AE results depend on various parameters, such as AE sensor, pre-amplification and hit detection, type of AE source, test set-up, specimen size, etc. Consequently, these conditions should be kept as similar as possible in order to make quantitative comparisons of the crack activity between different tests. Otherwise, the AE results can simply be used for qualitative comparisons of the activity.

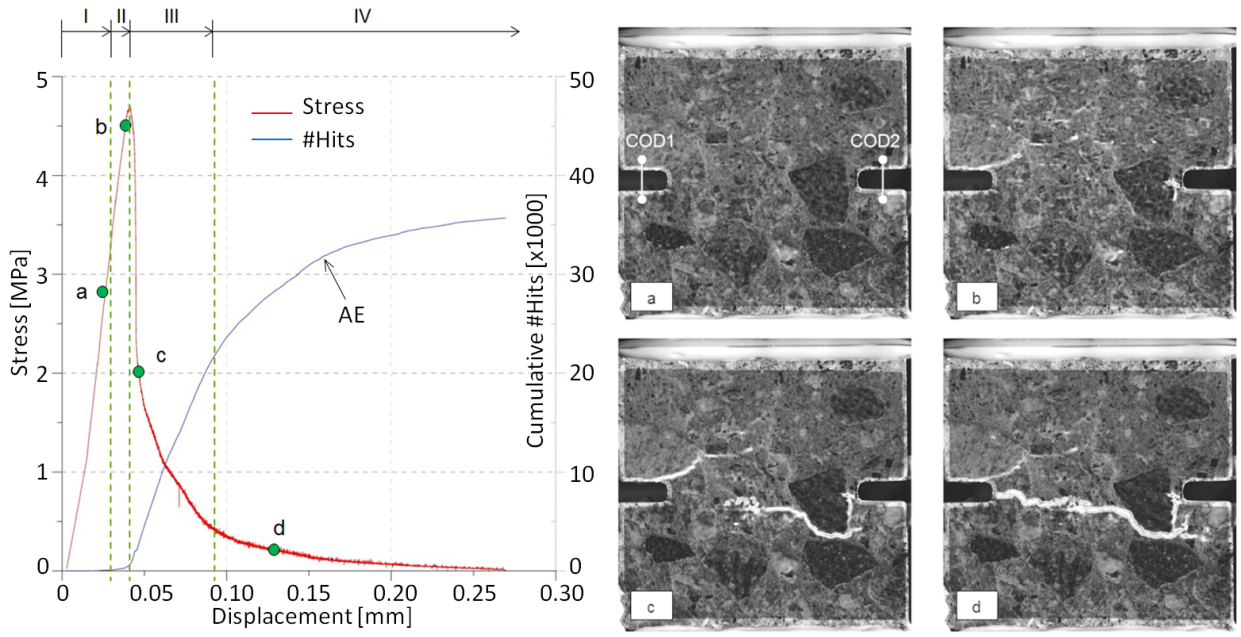

Figure 9 – Stress and cumulative AE Hits versus displacement (left) and example of crack formations in the different phases of the cracking process (right) for specimen C038-5. The image size is 65×65 mm^2.

The cracking process observed by DIC and AE during the tests may to some extent be related to different phases in the stress-displacement relationship. These findings correspond well with the four stages in the tensile fracture process defined in [26]; (I) elastic stage, (II) micro cracking, (III) macro cracking and (IV) bridging.

The cracking process is exemplified for one specimen (C038-5) in Figure 9 (right). Within the initial elastic pre-peak part (I) of the stress-displacement curve, the number of AE hits is small which is thought to be related to the opening of existing micro-cracks in both the cement matrix and the aggregate particles. These cracks are, however, difficult to identify by DIC but can be observed as successively appearing scattered deformations. When new cracks start to develop in phase II, mainly in the ITZ of the larger aggregate particles, the number of hits also starts to increase. The number of hits further increases when cracks start to propagate into the cement paste matrix from the ITZ or from the two notches. In the proximity of the peak stress, the crack intensity and resulting AE activity increase. These observations correspond well with the initiation of the non-linear behaviour, represented by an increasing curvature in the stress-displacement curve, which occurs just before peak stress is reached upon the merging of different micro-cracks. According to [26] this energy release in the pre-peak regime can be interpreted as the deviation from the "ideal" linear-elastic behaviour. During the post-peak

regime, the AE activity can be related to the energy needed to create the final fracture. The hit-rate reaches the highest value during the initial part of the post-peak behaviour related to the creation of one localized macro-crack in phase III. During the last phase (IV) of the post-peak behaviour related to gradual opening of the macro-crack, the AE activity is mainly caused by the bridging effect of the aggregate particles. While the crack opens, the hit rate decreases, and eventually becomes zero as the crack is completely open. The transitions between the different phases are, however, generally ambiguous and the phases are found to overlap.

Due to the scalable nature of DIC measurements, the cracks can be studied both with higher spatial resolution and higher displacement accuracy at the micro scale compared to the meso scale. Figure 10 presents the crack formations close to one of the notches at around maximum stress for C038-7 and N038-7, respectively. As can be observed, the cracks are mostly located in the ITZ and the cement matrix, but in some cases propagate through aggregate particles. A further development of surface preparation and lighting techniques would allow an improved spatial resolution of the cracks. Since the specimens had two notches, it was not possible to predict at which notch the main crack would be initiated and accordingly where to place the microscope.

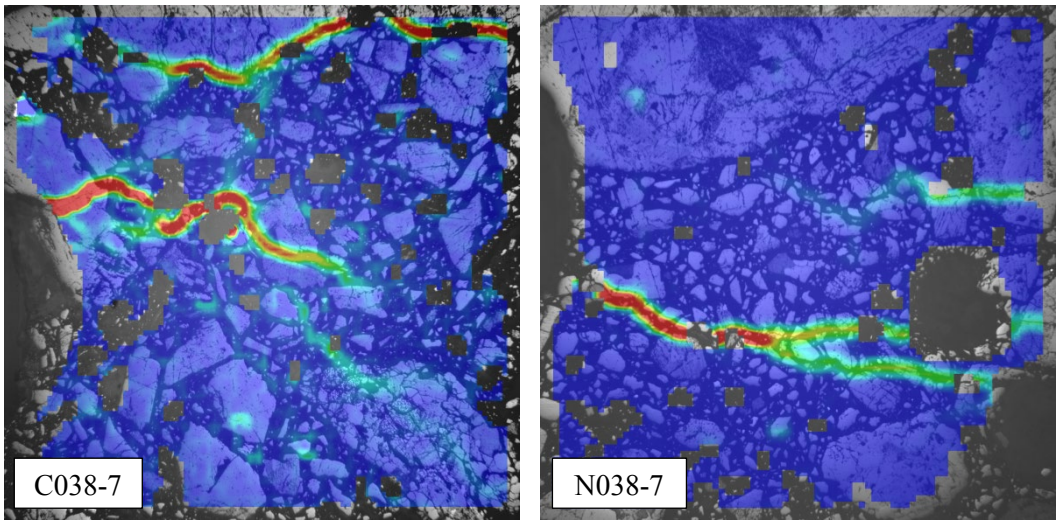

Figure 10 – Example of crack formations in C038-7 and N038-7, obtained by a microscopic lens. The notch can be seen to the left in both figures. The image size is 8×8 mm^2.

6. MICROSCOPIC ANALYSIS

After testing, the specimens were analysed using a thin section technique in fluorescence microscopy combined with image analysis. The thin sections covered the entire fracture area from notch to notch, see Figure 11. The combination of DIC measurements during testing and fluorescence microscopy after testing makes it possible to characterize and quantify the fracture down to a micrometre scale and relate it to the cracking process during loading.

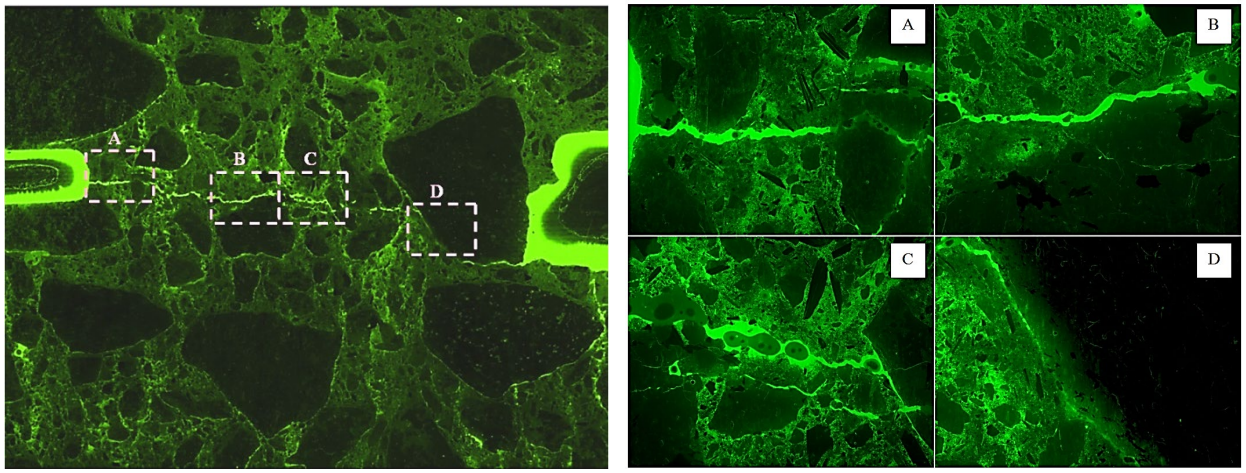

Figure 11 – Fluorescence image of C038-5 after testing, at meso (left) and micro scale (right). The meso scale image covers 50x40 mm^2 and the micro scale images cover 5.5x4.2 mm^2.

The fluorescence image shown in Figure 11 covers the area seen in the DIC images presented in Figure 9 (right). The approximate positions of the individual sub-images are indicated in Figure 11 (left). Sub-image (A) shows the area adjacent to the left notch. Sub-image (C) shows an area where the main fracture temporarily stopped during the test as can be seen in the DIC image (c) in Figure 9 (right). It can be observed that the microstructure is considerably damaged by the fracturing process in this region. Sub-image (D) shows the main fracture that was forced to go around the larger aggregate close to the right notch. It can be noted that the crack running diagonally from the left notch along the ITZ in Figure 9 (b) to (d) has to a large extent closed after the test, as can be seen in Figure 11 (left).

As described earlier, the fracture surfaces were classified as fractures in aggregate, in paste and in the ITZ. Figure 12 shows an example of this fracture classification for samples C038-8 and N038-6. The results from the measurements of total fracture length are given as percentages in Table 4, showing that the aggregate shape has no significant influence on the fracture propagation in tensile stage test. The fracture length distributions in paste, aggregate and ITZ are given in Table 5 and Figure 12.

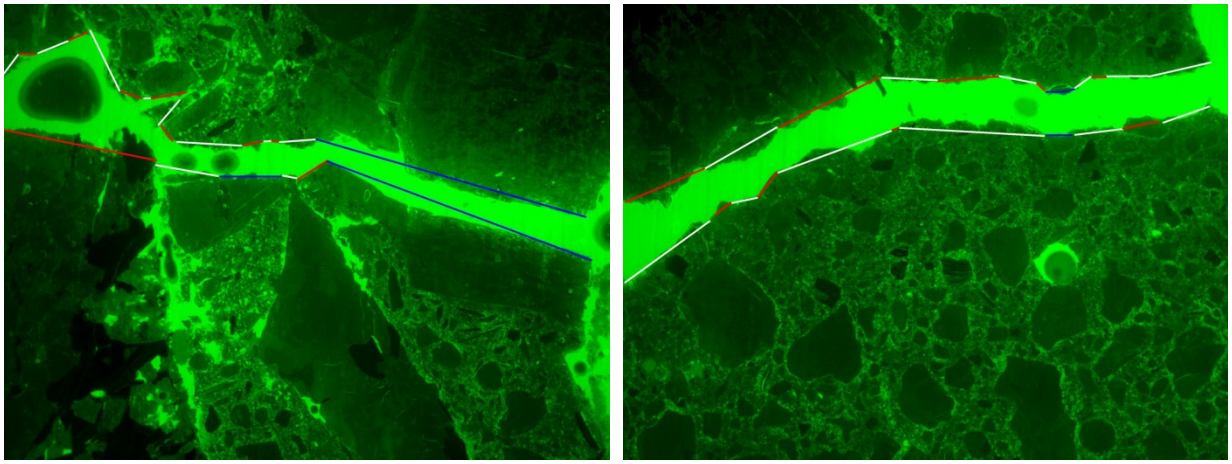

Figure 12 – Interpretation of fracture classification for sample a) C038-8 and b) N038-6. White line fracture in paste, red line adhesion and blue fracture in aggregate. The notch is seen to the right. The image covers 5.5x4.2 mm^2.

Table 4 – Quantitative results in % on crack propagation in the tensile stage tests.

	C038-5	C038-6	C038-8	N038-5	N038-6	N038-7	C038	N038
Aggregate	10	18	36	8	24	33	21	22
Paste	55	45	40	52	50	49	47	50
ITZ	35	37	24	40	26	18	32	28
Total	100	100	100	100	100	100	100	100

Table 5 – Fracture length distribution in aggregate (A), paste (P) and ITZ (T) as seen in Figure 12. Values given as percentages based on number of cracks in each size class.

Size [mm]	C038A	C038P	C038T	N038A	N038P	N038T
0.125	5	13	35	5	13	39
0.25	12	16	33	10	22	36
0.5	36	30	15	36	22	16
1	25	24	6	11	26	6
2	7	13	8	24	11	2
5	15	4	3	14	6	1
Total	100	100	100	100	100	100

A comparison with results obtained from tests in shear in a previous study using the same concrete [9] shows that the fracture process in shear is dependent on the shape of the aggregate particles which is not the case in tension as shown in this investigation. There are, however, differences in detail of the fracture pattern between samples with rounded natural aggregate and those with elongated crushed aggregate, also in tension. The analysis of fractures in tension shows that there are more secondary fractures branching out from the primary fracture in samples with crushed aggregate. Branching may form when a propagating crack reaches a void in the structure and several cracks are initiated on the opposite side of the void. Branching may also occur when a secondary crack propagates along the ITZ of an aggregate particle oriented oblique to the direction of propagation. The main crack continues in the cement paste along the main direction of propagation. If the propagating crack passes through or around an aggregate particle depends partly on its size and orientation as well as the presence of internal weaknesses in the particle. The influence of size can be seen in Table 5 where the cracks in the ITZ are mainly short while cracks through the aggregate particles are longer. Propagating secondary cracks often stop or are deflected at aggregate particles. It is suggested that this is more frequent in the samples with crushed aggregate. As the secondary fractures have partly grown in shear, flaky particles may act through interlocking. Aggregates deform in a more brittle manner compared to the cement paste and, as such, a more brittle fracture behaviour is expected if more of the crack propagation occurs in aggregates. This can be observed in the post peak behaviour of the samples N38-5 and C38-5 compared to N38-7 and C38-8, see Figure 7 and Table 4. The differences in meso and micro scales provide potential explanations for the observed differences in the mechanical behaviour. Accordingly, this research area is suitable for continued research.

7. CONCLUDING REMARKS

The development of a methodology, based on the combination of different experimental methods and measuring techniques on different levels of scales is presented. During direct tensile tests on small scale concrete specimens, the cracking process was registered by means of

DIC and AE. By combining DIC and AE, it was possible to visualize crack propagation and identify different phases of the cracking process both in the pre-peak and post-peak regimes, from micro-crack initiation to completion of the final fracture. Furthermore, the DIC measurements allow to locate cracks and also to quantify the crack opening displacement and the crack length by analysing discontinuities in the displacement field. Furthermore, this study indicates a strong correlation between the AE activity and the level of mechanical damage in the material, related to the crack formation.

After the direct tensile test, the cracks and final fractures were studied in detail using fluorescence microscopy, linking the cracking and fracturing process to the material structure of the concrete. The applied combination of methods provides detailed information of the cracking process. Hence, the present project shows that the applied combination of methods has a potential for increasing the understanding of cracking process on micro and meso scale and how it relates to the loading. This makes it a useful approach for the study of new cement based materials.

According to the analysis, there are no major differences in the fracture behaviour in tension between concrete with crushed compared to natural sand in the aggregate finer than 8 mm. This observation differs from the behaviour in shear wherein the shape of the aggregate had a distinct influence.

REFERENCES

1. Rouchier S, Foray G, Godin N, Woloszyn M and Roux J-J: Damage monitoring in fibre reinforced mortar by combined digital image correlation and acoustic emission. *Construction and Building Materials*, Vol. 38, 2013, pp. 371-380.
2. Alam S Y, Saliba J and Loukili A: Fracture examination in concrete through combined digital image correlation and acoustic emission techniques. *Construction and Building Materials*, Vol. 69, 2014, pp. 232-242.
3. Guo M, Alam S Y, Bendimerad A Z, Grondin F, Rozière E and Loukili A: Fracture process zone characteristics and identification of the micro-fracture phases in recycled concrete. *Engineering Fracture Mechanics*, Vol. 181, 2017, pp. 101-115.
4. Caduff D and van Mier J G M: Analysis of compressive fracture of three different concretes by means of 3D-digital image correlation and vacuum impregnation. *Cement and Concrete Composites*, Vol. 34, No. 4, 2010, pp. 281-290.
5. Sutton M A, Orteu J J and Schreier H W: *Image correlation for shape, motion and deformation measurements*. 2009, Springer, New York.
6. Destrebecq J F, Toussaint E and Ferrier E: Analysis of cracks and deformations in a full scale reinforced concrete beam using a digital image correlation technique. *Experimental Mechanics*, Vol. 51, No. 6, 2010, pp. 879–890.
7. Skoček J and Stang H: Application of optical deformation analysis system on wedge splitting test and its inverse analysis. *Materials and Structures*, Vol. 43, 2010, pp. 63–72.
8. Shah S P and Chandra Kishen J M: Fracture properties of concrete-concrete interfaces using digital image correlation. *Experimental Mechanics,* Vol. 51, No. 3, pp. 303–313.
9. Flansbjer M, Lindqvist J E and Silfwerbrand J: Quantitative fracture characteristics in shear load. *Proceedings*, *fib* Symposium, Prague, Czech Republic, 8-10 June 2011, pp. 567-570.
10. Jacobsen J S, Poulsen P N and Olesen J F: Characterization of mixed mode crack opening in concrete. *Materials and Structures*, Vol. 45, 2012, pp. 107-122.

11. Skarżyński L, Kozicki J and Tejchman J: Application of DIC technique to concrete – Study on objectivity of measured surface displacements. *Experimental Mechanics,* Vil. 53, 2013, pp. 1545–1559.
12. Gencturk B, Hossain K, Kapadia A, Labib E and Mo Y-L: Use of digital image correlation technique in full-scale testing of prestressed concrete structures. *Measurement*, Vol. 47, 2014, pp. 505–515.
13. De Wilder K, Lava P, Debruyne D, Wang Y, De Roeck G and Vandewalle J: Experimental investigation on the shear capacity of pre-stressed concrete beams using digital image correlation. *Engineering Structures*, Vol. 82, 2015, pp. 82–92.
14. Hamrat M, Boulekbache B, Chemrouk M and Amziane S: Flexural cracking behavior of normal strength, high strength and high strength fiber concrete beams, using Digital Image Correlation technique. *Construction and Building Materials*, Vol. 106, 2016, pp. 678–692.
15. Grosse C U and Ohtsu M: *Acoustic Emission Testing*, Springer-Verlag, Berlin, Heidelberg, 2008.
16. Ohno K and Ohtsu M: Crack classification in concrete based on acoustic emission. *Construction and Building Materials*, Vol. 34, 2010, pp. 2339-2346.
17. Fricker S and Vogel T: Site installation and testing of continuous acoustic monitoring. *Construction and Building Materials*, Vol. 21, 2007, pp. 501-510.
18. Kencanawati N N, Iizasa S and Shigeishi M: Fracture process and reliability of concrete made from high grade recycled aggregate using acoustic emission technique under compression. *Materials and Structures*, Vol. 46, 2013, pp. 1441-1448.
19. Soulioti D, Barkoula N M, Paipetis A, Matikas T E, Shiotani T and Aggelis D G: Acoustic emission behavior of steel fibre reinforced concrete under bending. *Construction and Building Materials*, Vol. 23, 2009, pp. 3532-3536.
20. Muralidhara S, Raghu Prasad B K, Hamid Eskandari and Karihaloo B L: Fracture process zone size and true fracture energy of concrete using acoustic emission. *Construction and Building Materials*, Vol. 24, 2010, pp. 479-486.
21. Saliba J, Loukili A, Grondin F and Regoin J P: Identification of damage mechanisms in concrete under high level creep by the acoustic emission technique. *Materials and Structures*, Vol. 47, 2014, pp. 1041-1053.
22. NT BUILD 486: *Aggregates: Size distribution*. Approved 1998-11, NT BUILD.
23. Lindqvist J E and Johansson S: Aggregate shape and orientation in historic mortars. *Proceedings,* 11th Euroseminar Applied to Building Materials, Ed I Fernandes, 2007.
24. RILEM TC 187-SOC: *Experimental determination of the stress-crack opening curve for concrete in tension: Final report*, May 2007.
25. RILEM TC 162-TDF: Test and design methods for steel fibre reinforced concrete: Uni-axial tension test for steel fibre reinforced concrete. *Materials and Structures*, Vol. 34, 2001, pp. 3-6.
26. van Mier J G M: *Concrete Fracture, a Multiscale Approach*, CRC Press, 2012.